TECHNICAL ARTICLE

Insight into the Corrosion Resistance of Plasma Electrolytic Oxidation (PEO) Mg Alloys from the Microstructures in PEO Coatings

Zhenning Chen, Xiaoqian Geng, Xingyue Yong, and Xiaochun Chen

The microstructures in the thickening of plasma electrolytic oxidation (PEO) coatings and their effects on the corrosion resistance of the PEO Mg alloys were investigated using x-ray tomography in conjunction with electrochemical impedance spectroscopy (EIS). It was found that the micropores would develop and connect with each other in the thickening of PEO coatings, resulting in the increment of the average diameters and the maximum diameters of the micropores. The thickness of the whole PEO coating gradually increased with oxidation time, and it was beneficial to diminish the through-pores in PEO coatings. The PEO Mg alloy prepared by controlling 40 min oxidation time exhibited the best corrosion resistance because of its larger thickness, denser structure, and higher content of the Mg_2SiO_4 phase in the PEO coating. Based on equivalent circuits for EIS spectra, the limit value of the low-frequency resistance (R_l) was used to evaluate the corrosion resistance of the PEO Mg alloys. And that this method was verified by the experimental results.

1. Introduction

Recently, various kinds of surface treatment techniques (Ref 1-5), such as chemical conversion, electrodeposition, vapor deposition, and anodizing, have been developed to improve the corrosion resistance of Mg and its alloys. Among these techniques, plasma electrolytic oxidation (PEO) has become a potential technique because PEO coatings have relatively good wear resistance, corrosion resistance, and high thermal stability (Ref 6). However, it was found that the micro-cracks and micropores existed in PEO coatings (Ref 7) and that these micro-defects were harmful to the barrier properties of PEO coatings (Ref 8).

Generally, micro-defects inevitably exists in various corrosion-resistant films/coatings, such as passive films (Ref 9, 10), conversion layers (Ref 11-13), and organic coatings (Ref 14-16). These micro-defects always become pathways for the transportation of corrosive media to the coating/substrate interface, resulting in the occurrence of localized corrosion of the metallic substrate (Ref 17-20). For instance, the micro-defects (vacancies, wrinkles, and cracks) (Ref 21, 22) in graphene coatings accelerated corrosion of coated metals

compared with uncoated metals (Ref 23, 24). Similarly, the micro-defects in thermal spraying coatings impaired their corrosion resistance (Ref 25, 26). It was also found that the micropores in PEO coatings would provide pathways for the transportation of corrosive media to the coating/substrate interface, leading to the premature failure of PEO coatings (Ref 27). Our previous studies (Ref 28) also showed that the localized corrosion of a PEO Mg alloy was mainly attributed to the transportation of corrosive media to the coating/substrate interface through these micro-defects in the PEO coating. Up to date, various post-treatment methods has been proposed to seal the micro-defects in the PEO coating (Ref 29-31), including chemical conversion, hydrothermal treatment, organic coating, particles addition, etc. However, there were some unsealed micropores in the PEO coating. Thus, these unsealed micropores would still provide transportation paths for corrosive media, finally they became the origin that may induce the failure of the silane-treated PEO coating. Therefore, it is important to study the microstructures in the growth of the PEO coating and its effects on the corrosion resistance of PEO Mg alloys so as to improve the PEO process and understand the relationship between the microstructures of PEO coatings and the corrosion resistance of PEO Mg alloys.

In the past years, some researchers studied the corrosion resistance of PEO Mg alloys (Ref 32-35) and the 2D surface and cross-sectional morphologies of PEO coatings (Ref 32, 36, 37). However, the traditional methods cannot be used to study the micro-shapes and distribution of the micro-defects in PEO coatings in the 3D space. X-ray tomography (XRT) is a nondestructive 3D detecting technique and has been successfully used to investigate the 3D microstructures of materials (Ref 38). Recently, XRT has been used to study the 3D microstructures of PEO coatings (Ref 39, 40). To the best of the authors' knowledge, few studies were focused on the relation-

Zhenning Chen, Xiaoqian Geng, Xingyue Yong, and **Xiaochun Chen**, State-Key Laboratory of Organic-Inorganic Composites, Beijing University of Chemical Technology, North Third Ring Road 15, Beijing 100029, China. Contact e-mail: yongxy@mail.buct.edu.cn.

ship of the 3D microstructures of PEO coatings with the corrosion resistances of PEO Mg alloys.

In this study, x-ray tomography (XRT) was used to study the 3D microstructural characteristics of PEO coatings prepared by controlling different oxidation times. At the same time, electrochemical impedance spectroscopy (EIS) was used to evaluate the corrosion resistance of PEO Mg alloys to investigate the relationship between the 3D microstructure of PEO coatings and the corrosion resistance of PEO Mg alloys.

2. Materials and Experimental Methods

In this study, samples of ZM6 Mg alloy were used as the substrate, the chemical compositions of which are listed in Table 1. The PEO specimens were prepared using a PEO device under a constant current control mode with a fixed current density of 80 mA/cm^2. The frequency and duty ratio were 500 Hz and 40%, respectively. The electrolyte, which was mainly composed of 11 g/L Na_2SiO_3, 2 g/L NaOH, 2 g/L NaF, and 5 g/L glycerine, was placed in the cylinder container. During plasma electrolytic oxidation, the electrolyte was continuously stirred; the temperature was controlled at 20 ± 5 °C by a circulating water-cooling system. The different PEO coatings were prepared by controlling different oxidation times. The PEO Mg-alloy specimens with different thicknesses were obtained by controlling 5, 15, 25, and 40 mins of oxidation time and were designated as coating A, B, C, and D, respectively.

The surface and the cross-sectional morphologies of the PEO specimens were examined by scanning electron microscopy (SEM) (JEOL JSM-7800F, Japan). The sizes of the open pores on the surface of PEO coatings were calculated using Nano-Measure software. The 3D surface morphologies of PEO specimens were observed by confocal laser scanning microscopy (CLSM) (Olympus LEXTOLS4000, Japan). The CLSM images (view field: 130 μm × 130 μm) were analyzed by the LEXT software (version 2.2, Olympus, Japan). The surface roughness of PEO coatings was accomplished by the surface roughness measurement module using the LEXT software. X-ray tomography (XRT) measurements were taken using the ZEISS Xradia 500 Versa system to investigate the 3D shapes and distribution of micro-defects in the different PEO coatings. The view field of the XRT images was 230 μm × 350 μm. The coating porosity, pore sizes, and pore numbers were analyzed using the Avizo 7.1 software. Additionally, the thicknesses of different PEO coatings were measured using an Elcometer apparatus. The average thickness values were calculated based on the measurement values of 10 points.

The chemical structures of PEO coatings were investigated by x-ray diffraction (XRD) (UItimaIII, Japan) with the monochromated Cu-Ka radiation from $2\theta = 5°$ to $2\theta = 90°$.

The obtained XRD spectra were analyzed using Jade 6.5 software.

Open circuit potential (OCP) and electrochemical impedance spectroscopy (EIS) of PEO specimens in a 3.5 wt.% NaCl solution (pH = 7.0) were measured with an electrochemical workstation (Gamry 600 plus, USA). The 3.5 wt.% NaCl solution was chosen to simulate an aggressive environment containing chlorides. The A three-electrode cell was used for the impedance measurements. The saturated calomel electrode (SCE) was used as the reference electrode, and the platinum electrode was used as the counter electrode. The tested area of a PEO specimen was 6 cm^2. Before the electrochemical tests, the sample was immersed in a 3.5% NaCl solution for 20 min. for OCP stabilization. The tests were repeated three times. The frequency range was from 10^{-2} to 10^5 Hz with an AC perturbation of 5 mV. The obtained EIS data were firstly tested by Kramers–Kronig transforms. EIS spectra were then fitted using Gamry Echem Analyst software based on the equivalent circuits to obtain electrochemical parameters.
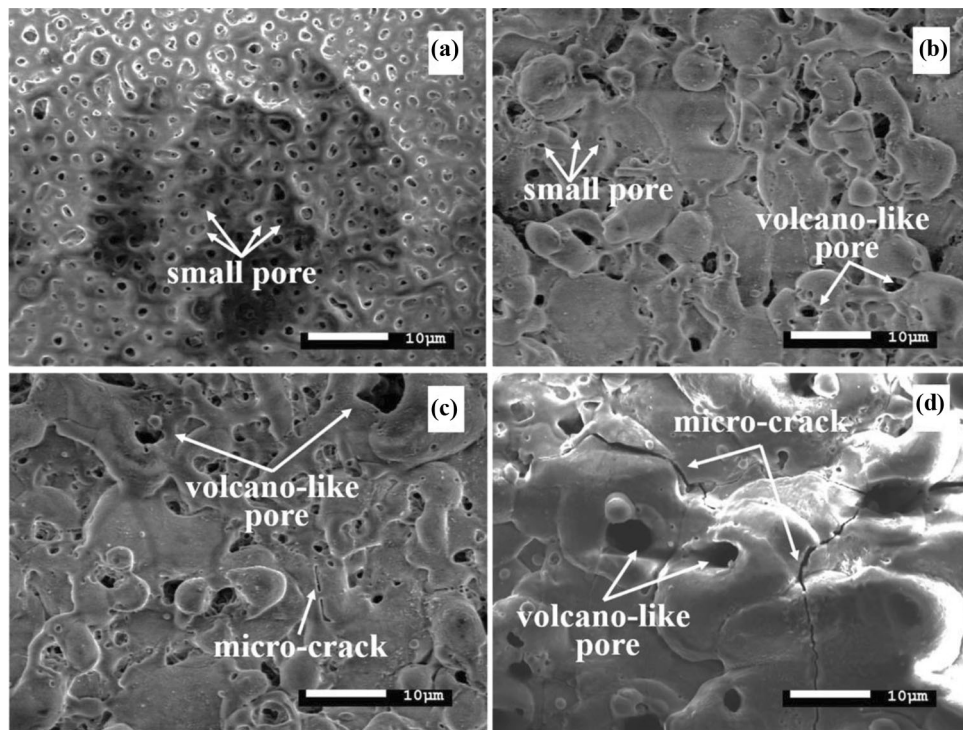
3. Results and Discussion

3.1 Microstructural Characteristics of PEO Coatings

In this study, the microstructural characteristics of different PEO coatings were investigated using SEM, CLSM in conjunction with XRT techniques. The results are shown in Fig. 1, 2, 3 and 4.

3.1.1 2D Morphologies of PEO Coatings. Figure 1 shows that the PEO coatings prepared by controlling different oxidation times had different surface morphologies. Some micropores and micro-cracks were observed on the surfaces of PEO coatings. The diameters of the open pores on the surface of the PEO coating A, B, C, and D were 0.1-2.7 μm, 0.1-3.4 μm, 0.1-5.8 μm, and 0.1-7.5 μm, respectively. The number of micro-cracks and volcano-like pores increased with oxidation time. Figure 2 also shows that the maximum height difference of the coating surfaces increased with oxidation time. This was probably associated with stronger discharge events (Ref 41). It was further indicated that the PEO coatings prepared by controlling different oxidation times would have different microstructural characteristics.

The SEM images of the cross section of PEO coatings are shown in Fig. 3. It was found that the thicknesses of PEO coatings gradually increased with oxidation time; the boundary between the inner layer and outer layer of PEO coatings tended to be much more obvious. Some micropores were distributed along the thickness direction of PEO coatings. Through-types of micropores were observed in coating A (Fig. 3a); micro-cracks were observed in coating B, C, and D (Fig. 3b–d). It was indicated that the increment of the thickness of a PEO coating would be beneficial to reduce the existences of through-pores in the PEO coatings, i.e., the increment of oxidation time would be useful to diminish the through-pores in the PEO coatings. By comparison, coating A would have a poor corrosion resistance when it was exposed to corrosive environments and Coating D would probably have a better corrosion resistance.

3.1.2 3D Micro-Shapes of Micro-Defects in PEO Coatings. The 3D XRT images of PEO coatings are shown in Fig. 4. The micropores with different sizes and shapes existed

Table 1 The chemical compositions (wt.%) of ZM6 Mg alloy

Nd	Zn	Zr	Cu	Ni	Mg
2.76	0.36	0.46	0.016	0.023	Balance

Fig. 1. SEM surface morphologies of PEO coatings (a) coating A; (b) coating B; (c) coating C; (d) coating D
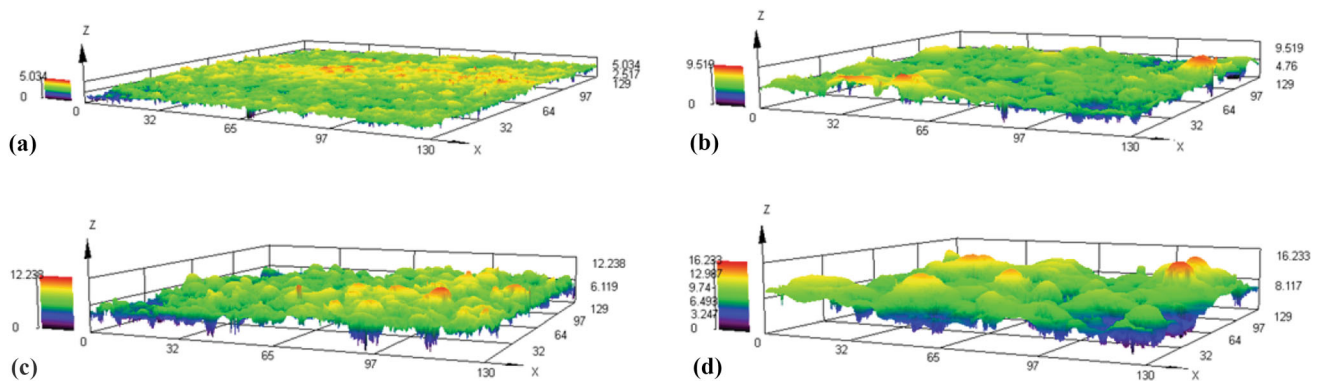
Fig. 2. CLSM surface morphologies of PEO coatings (a) coating A; (b) coating B; (c) coating C; (d) coating D

randomly in coating A, B, C, and D. The sizes of some micropores became larger and some of the micropores joined together with oxidation time due to the occurrence of the continuously stronger discharge (Ref 41). This was in accordance with results obtained by previous works of (Ref 39). The distribution of micropores in coating A was inhomogeneous; the micropores in the PEO coating B, C, and D tended to distribute uniformly with increasing oxidation time. It was found from the zoomed images in Fig. 4 that small micropores looked relatively high sphericity, and the larger micropores looked low sphericity and looked like a long capsule. This was consistent with the results of Ref 40. It should be noted that micro-cracks were not detected in PEO coatings, due to the resolution limitation of XRT.

3.1.3 Distribution of the Micro-Defects in PEO Coatings. Based on the calculations of these CLSM and XRT results, the quantitative distribution characteristics of the micro-

defects in PEO coatings were studied and are shown in Fig. 5.

As shown in Fig. 5(a), the average thicknesses of PEO coatings increased with oxidation time; the surface roughness of PEO coatings was increased and the number of micropores in PEO coatings decreased with oxidation time; the global porosity of coating C was the highest. It was indicated that the microstructural characteristics of PEO coatings were closely related to the micro-shapes and distribution of the micro-defects in the thickening of PEO coatings.

It can be seen from Fig. 5(b) that the local porosity increased exponentially along the thickness direction of the PEO coatings from the coating-substrate interface to the PEO coating surface. However, the porosity of the surface layer of coating B, C, and D decreased a little. This may be related to the surface shrinkage resulting from the quenching by the electrolyte (Ref 39, 40). If the layer with a below 3% porosity was considered as the compact inner layer, the thickness of the compact inner layer increased with oxidation time. This was due to that the
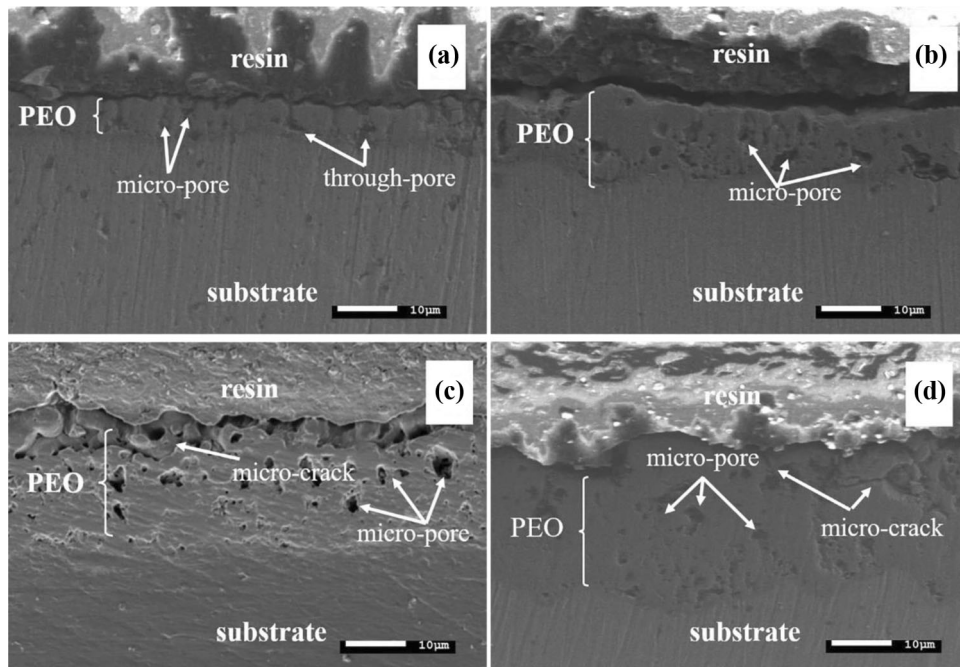
Fig. 3. SEM cross-sectional morphologies of PEO coatings (a) coating A; (b) coating B; (c) coating C; (d) coating D

inner layer grew faster than the outer layer and the melted material flowed back after the coating reached a certain thickness (Ref 42, 43). Therefore, the porosity of along the thick directions of different PEO coatings changed with oxidation time.

As shown in Fig. 5(c), the small-sized micropores had a higher percentage in PEO coatings. There were 85.0, 72.0, 70.5, and 70.8% of micropores with below 3 μm diameters in coating A, B, C, and D, respectively. At the same time, the average diameters of the micropores in PEO coatings increased with oxidation time. This was associated with the increment of coating thickness and the stronger discharge events.

3.2 Chemical Compositions of PEO Coatings

XRD measurements were taken to detect the chemical compositions of different PEO coatings. XRD spectra are shown in Fig. 6. It was deduced that there existed MgO (pdf: 71-1176), Mg_2SiO_4 (pdf: 71-1083), Mg (pdf: 89-7195), and $Mg_{0.97}Zn_{0.03}$ (pdf: 65-4596) in PEO coatings. And that MgO and Mg_2SiO_4 were the main chemical compositions of PEO coatings. Mg is a basic element of the Mg alloy substrate and $Mg_{0.97}Zn_{0.03}$ is a chemical phase in the Mg alloy substrate. The peaks of MgF_2 (pdf: 72-1150) were observed in coating A. The peaks of Mg and MgF_2 decreased gradually with oxidation time, showing that the content of MgF_2 is relatively lower in the outer layer (Ref 42, 43). Additionally, the new peaks of Mg_2SiO_4 (pdf: 71-1083) were found in coating C and D; the peak intensity of the Mg_2SiO_4 in coating D became stronger, indicating that the content of the Mg_2SiO_4 phase in PEO coatings would become higher with oxidation time. These results were consisted with the works of Ref 37. This may be attributed to the accelerated formation of Mg_2SiO_4 at the high temperature induced by the stronger discharge events (Ref 44). Under this condition, the formation of the thermodynamically stable Mg_2SiO_4 would be beneficial to improve the corrosion resistance of PEO coatings.

3.3 Corrosion Resistance of PEO Coatings

To evaluate the corrosion resistance of different PEO coatings, the measurements of OCP and EIS of PEO Mg alloy specimens were taken in a 3.5 wt.% NaCl solution. The results are shown in Fig. 7 and 8.

3.3.1 OCP Changes. Figure 7 shows the OCP of PEO specimens in a 3.5% NaCl solution as a function of immersion time. At the initial stage of immersion, the OCP values of PEO specimens increased rapidly. This may be related to the formation of $Mg(OH)_2$ on the surface of PEO specimens (Ref 28). Afterward, the OCP values decreased and showed a different degree of oscillation with immersion time. This may be attributed to the transportation of corrosive media through micro-defects in PEO coatings. Additionally, the pits were observed by visual inspection on the surfaces of these specimens at different immersion times. The first pit was observed on the surfaces of coating A, B, C, and D after immersion for about 5 min, 29 h, 25 h, and 40 h, respectively. Thus, the corrosion resistance of these PEO specimens obtained by controlling different oxidation times would be initially ranked as: coating D > coating B > coating C > coating A.

3.3.2 EIS Characteristics. EIS has been widely used to study the kinetics of electrochemical processes, chemical processes, or transportation processes (Ref 45-47). In this study, EIS measurements were taken to investigate the corrosion resistance of PEO specimens in a 3.5% NaCl solution. The results are shown in Fig. 8.

Figure 8a shows that the EIS spectrum of the specimen with coating A was composed of a depressed capacitive loop in the high- and medium-frequency regions and an inductive loop in the low-frequency region after 1h of immersion. There were three time constants. The equivalent circuit is described in Fig. 9a. R_s and R_{cp} represented the solution resistance and the resistance of solution in the through-pores, respectively. The existence of the inductive loop meant that the localized corrosion occurred at the exposed substrate surface (R_L, L)
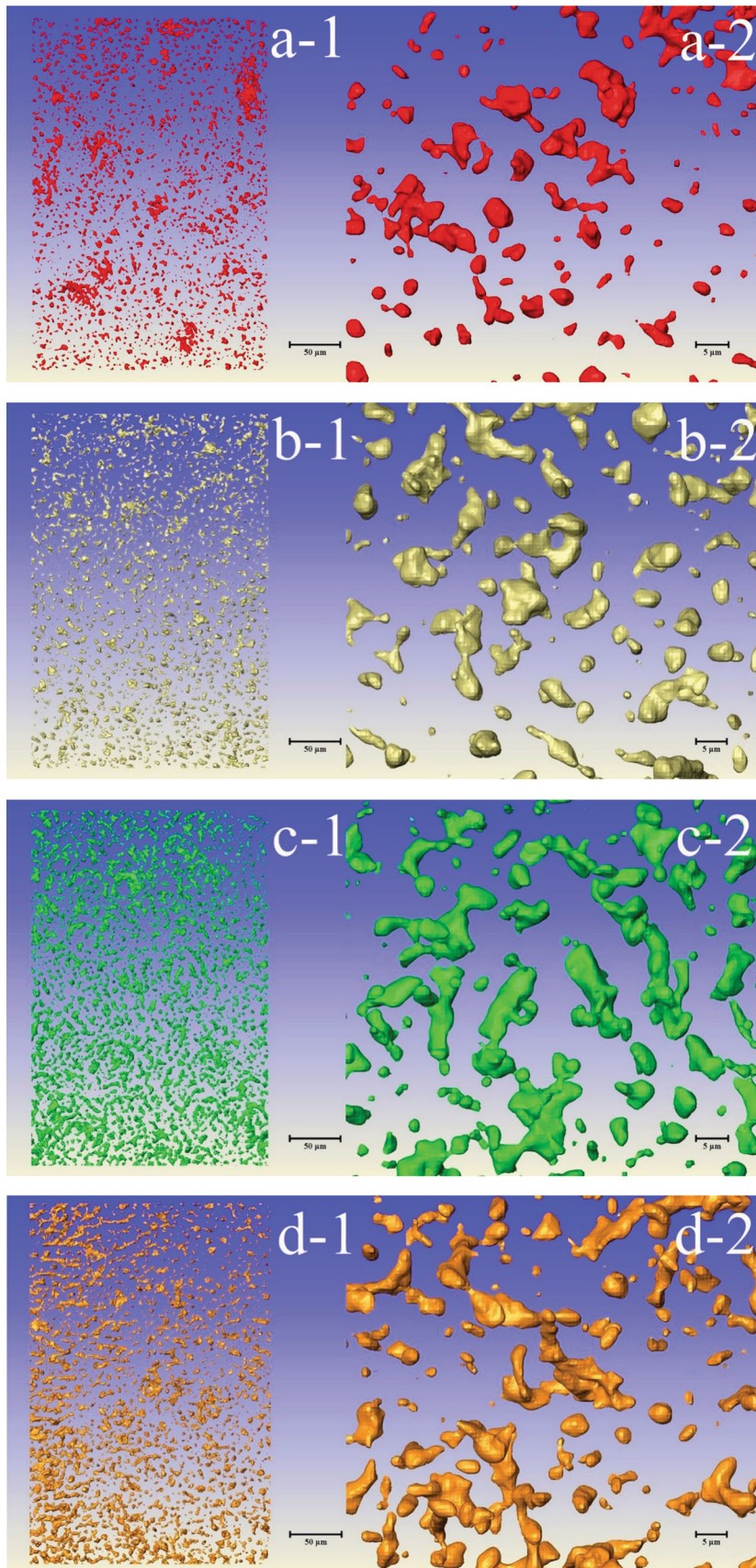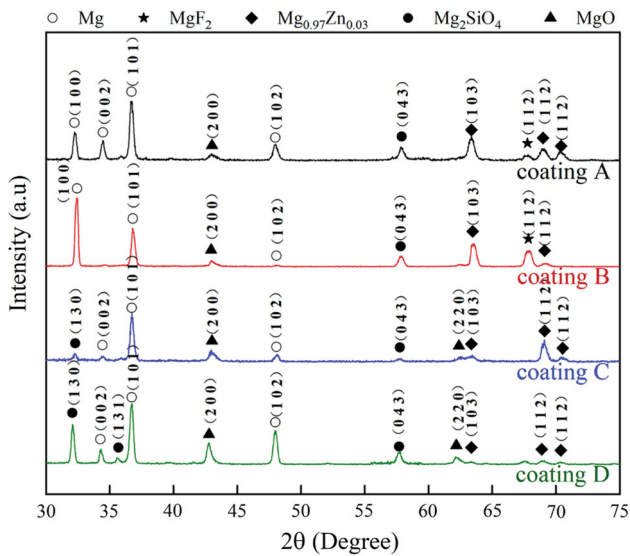
Fig. 4. XRT 3D morphologies of micro-defects in PEO coatings (a) coating A; (b) coating B; (c) coating C; (d) coating D
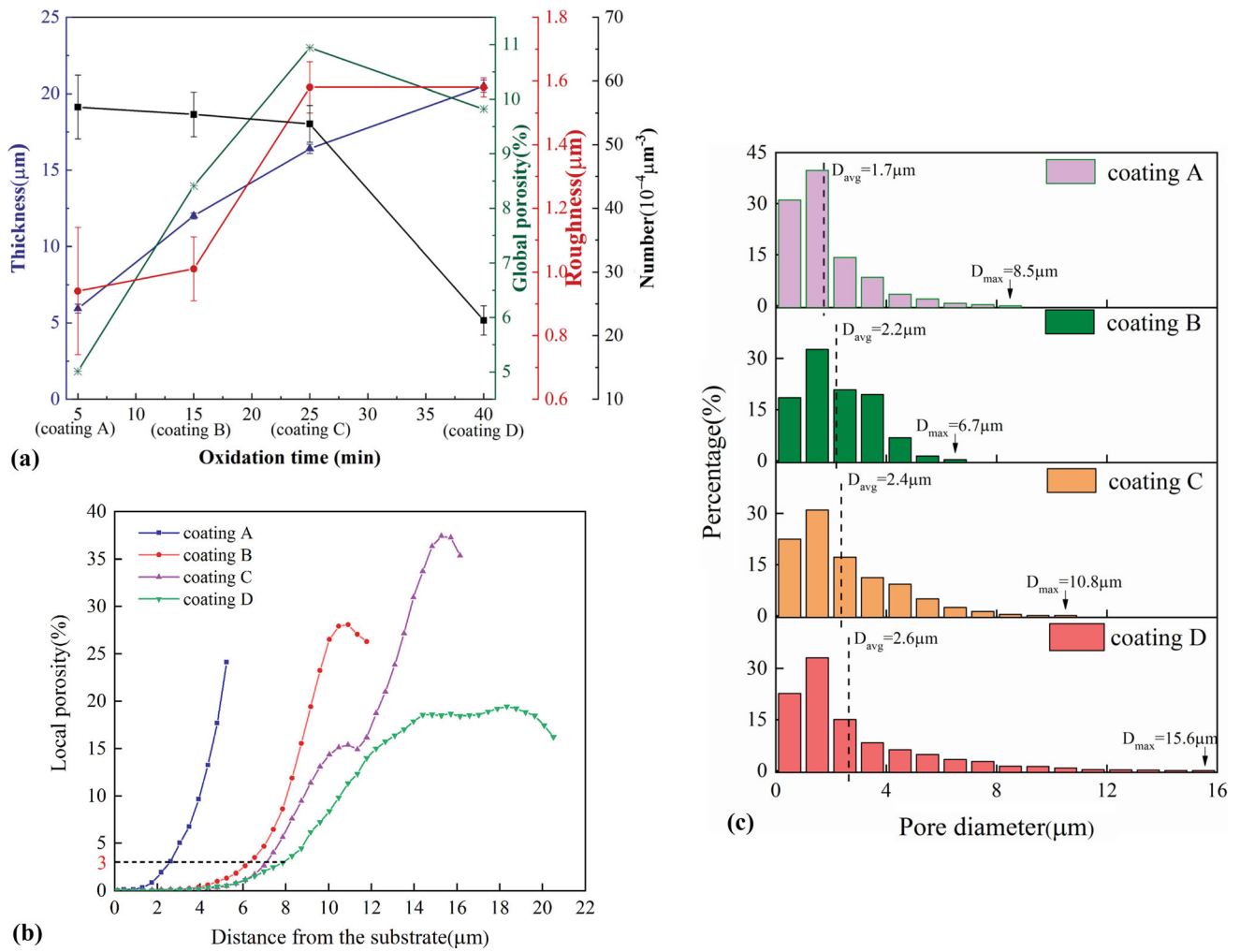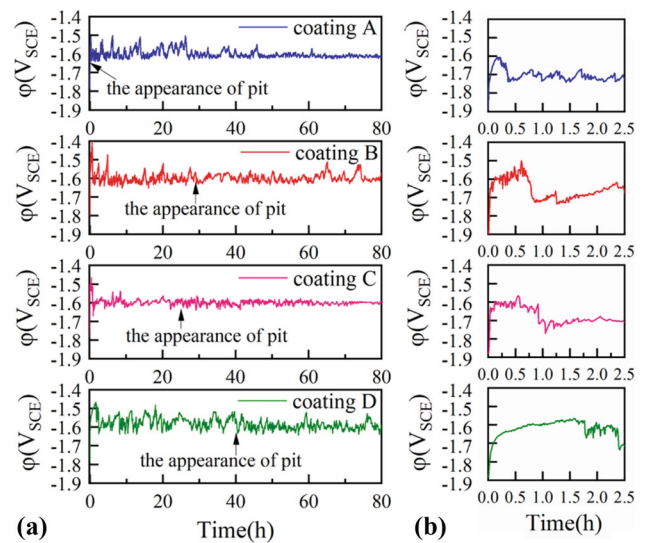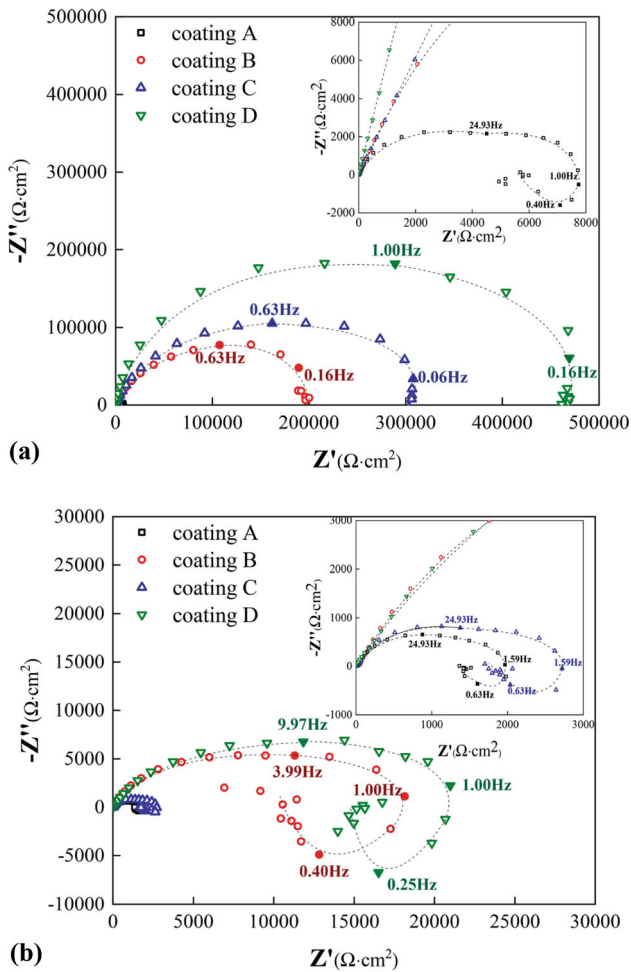
Fig. 5. Quantitative analysis of PEO coatings (a) coating parameters; (b) local porosity along the thickness direction; (c) distributions of the micropores

Fig. 6. XRD patterns of the PEO Mg-alloys

Fig. 7. OCPs of the PEO Mg alloy in a 3.5% NaCl solution as a function of immersion time (a) OCP as a function of immersion time; (b) zoomed images of OCPs at the initial immersion stage
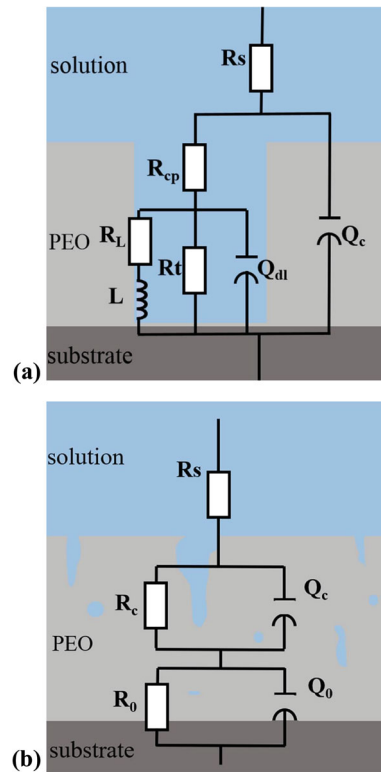
Fig. 8. EIS spectra of the PEO Mg alloys in a 3.5% NaCl solution (a) immersion for 1h; (b) immersion for 50 h

Fig. 9. Equivalent circuits based on the EIS spectra in Fig. 8

(Ref 48-50). R_L and L symbolized the resistance and inductance of the electrochemical reaction. The depressed capacitive loop was related to the PEO coating (Q_c, R_{cp}) and the exposed substrate at the bottom of the through micropores (Q_{dl}, R_t). Q_c and Q_{dl} represented the CPE element of the MAO coating and the double layer, respectively. R_t was the charge-transfer resistance of pitting corrosion. Due to the existence of through-pores in coating A, the total electrochemical impedance (Z_T) of the specimen with coating A was equal to the impedance of the coating (Z_c) in parallel with the impedance of the exposed substrate (Z_t). That is

$$\frac{1}{Z_T} = \frac{1}{Z_c} + \frac{1}{Z_t}. \tag{Eq 1}$$

Finally, the measured impedance of the specimen was approximately equal to the impedance (Z_t) of the exposed substrate, due to that the coating impedance (Z_c) was much higher than that of the exposed substrate (Z_t). In this case, the EIS spectrum showed the electrochemical characteristics of the exposed substrate of the specimen with coating A.

However, the EIS spectra of the specimens with coating B, C, and D were a depressed capacitance loop with two time constants (Fig. 8a). The depressed capacitive loop was related to the PEO coating (Q_c, R_c) and the coating/substrate interface (Q_0, R_0). The equivalent circuit is shown in Fig. 9(b).

When the immersion time was up to 50 h, as shown in Fig. 8(b), the EIS spectra of these specimens were composed of a depressed capacitance loop in the high- and medium-frequency regions and an inductive loop in the low-frequency region, suggesting that localized corrosion occurred to these PEO specimens. The diameters of the capacitive loops became much smaller compared with that of the spectra at the initial immersion stage, indicating that corrosion resistance decreased significantly. The equivalent circuit was the same as shown in Fig. 9(a).

3.3.3 Electrochemical Parameters. In this study, the electrochemical parameters were obtained by fitting the EIS spectra in accordance with the equivalent circuits in Fig. 9. The fitting results are listed in Tables 2 and 3.

As listed in Table 2, the charge-transfer resistance (R_t) was 5.55×10^4 Ω cm^2 after the specimen with coating A immersed in a 3.5 wt.% NaCl solution for 1 h. Q_{dl} was higher than Q_c, and both n_{dl} and n_c were lower than 0.9, showing the inhomogeneity of coating A and the occurrence of the localized corrosion at the coating/substrate interface. It can be seen from Table 3 that both R_c and R_0 increased with oxidation time after these specimens with coating B, C, and D were immersed in a 3.5 wt.% NaCl solution for 1h. This was associated with the larger thicknesses of PEO coatings and the higher content of the thermodynamically stable phase (Mg$_2$SiO$_4$) in PEO coatings. Therefore, the corrosion resistance of PEO coatings increased in the thickening of PEO coatings. This was also consisted with the literature (Ref 6, 30). R_0 was much larger than R_c, indicating that the coating/substrate interface kept good corrosion resistance at the initial immersion stage. Compared with R_{cp} of the specimen with coating A, R_c values of these specimens with coating B, C, and D were much higher, showing that these specimens with coating B, C, and D had a better corrosion

Table 2 Electrochemical parameters based on the equivalent circuit in Fig. 9(a)

	R_s, Ω cm^2	Q_c, S cm^{-2} s^{-n}	n_c	R_{cp}, Ω cm^2	Q_{dl}, S cm^{-2} s^{-n}	n_{dl}	R_t, Ω cm^2	R_L, Ω cm^2	L, H cm^2
Coating A-1h	12.24	3.63×10^{-7}	0.85	1.19×10^2	4.49×10^{-7}	0.87	5.55×10^4	2.01×10^5	2.08×10^{-2}
Coating A-50 h	26.74	3.06×10^{-6}	0.81	5.39×10^1	3.51×10^{-6}	0.83	3.53×10^4	1.56×10^4	2.50×10^{-2}
Coating B-50 h	13.80	1.01×10^{-6}	0.85	4.83×10^2	5.57×10^{-7}	0.87	5.55×10^4	1.34×10^4	1.58×10^{-2}
Coating C-50 h	15.97	1.51×10^{-6}	0.83	5.96×10^1	2.21×10^{-6}	0.89	6.69×10^4	2.03×10^3	1.97×10^{-5}
Coating D-50 h	24.68	5.26×10^{-7}	0.85	1.63×10^3	3.27×10^{-7}	0.88	3.98×10^4	1.86×10^4	1.10×10^{-1}

Table 3 Electrochemical parameters based on the equivalent circuit in Fig. 9(b)

	R_s, Ω cm^2	Q_c, S cm^{-2} s^{-n}	n_c	R_c, Ω cm^2	Q_0, S cm^{-2} s^{-n}	n_0	R_0, Ω cm^2
Coating B-1h	13.01	3.11×10^{-6}	0.82	1.56×10^4	1.55×10^{-6}	0.86	1.87×10^5
Coating C-1h	11.63	1.27×10^{-6}	0.81	8.40×10^4	1.74×10^{-6}	0.85	2.33×10^5
Coating D-1h	19.17	5.97×10^{-7}	0.99	8.60×10^4	4.50×10^{-7}	0.90	3.93×10^5

resistance than that of the specimen with coating A at the initial immersion stage. In addition, n_c values of these specimens with coating A, B, C, and D were 0.85, 0.82, 0.81, and 0.99, respectively. It indicated that the inhomogeneity of the coating surface could be ranked as: coating C < coating B < coating A < coating D, which was associated with the porosity of the surface layer of the PEO coatings (see Fig. 5b).

After these specimens were immersed in a 3.5% NaCl solution for 50 h, the electrochemical parameters are listed in Table 2. It was found that the coating resistances decreased with immersion time because of the penetration of corrosive media in PEO coatings. Here, the limit value of the low-frequency impedance (R_l) was used to evaluate the corrosion resistance of PEO specimens with different PEO coatings. Thus,

$$R_l = \lim_{f \to 0} |Z|. \tag{Eq 2}$$

The R_l values of the equivalent circuits in Fig. 9 could be calculated as followings in accordance with Eq (2): for Fig. 9(a):

$$R_l = R_{cp} + \frac{R_t R_L}{R_t + R_L} \tag{Eq 3}$$

for Fig. 9(b):

$$R_l = R_c + R_0. \tag{Eq 4}$$

The R_l values of these PEO specimens are shown in Fig. 10. It was found that their corrosion resistance at the initial immersion stage could be ranked from the best to the worse: coating D > coating C > coating B > coating A. However, after these PEO specimens were immersed in a 3.5% NaCl solution for 50 h, their corrosion resistance could be ranked from the best to the worse: coating D > coating B > coating C > coating A. This was in good agreement with the OCP results. It was further demonstrated that there were obvious effects of the microstructures of PEO coatings on the corrosion resistance of PEO specimens. At the initial immersion stage, the corrosion resistance of PEO specimens increased with the increasing thicknesses of PEO coatings and the content of the thermodynamically stable compositions (Mg_2SiO_4) in PEO coatings. After PEO specimens had been immersed in a 3.5% NaCl solution for a longer time, the corrosion resistance of PEO
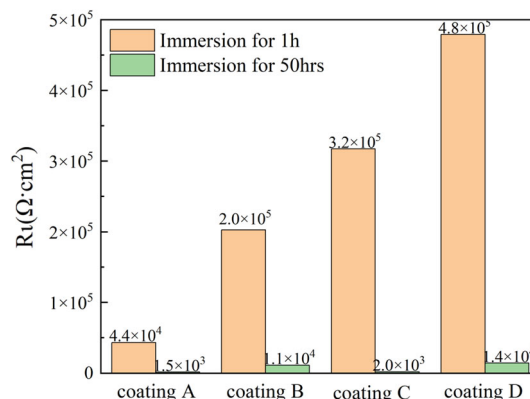
Fig. 10. R_l values of PEO specimens as a function of immersion time

coatings would be influenced by their porosities. This was verified by the morphologies of the PEO specimens after 50 h of immersion in a 3.5% NaCl solution (Fig. 11). It was seen from Fig. 11 that the numbers of corroded pits on the surfaces of coating A, B, C, D were different, showing that the different PEO coatings were subjected to different degrees of corrosion failure, the sequence of which could be ranked as: coating A > coating C > coating B > coating D. This further verified the above results.

In this study, based on the normal distribution model (Ref 51), the effective capacitance (C_{eff}) of PEO coatings could be calculated by the following formula:

$$C_{eff} = Q_c^{1/a} (R_c)^{(1-a)/a} \tag{Eq 5}$$

$$C_{eff} = \frac{\varepsilon_r \varepsilon_0 S}{d} \tag{Eq 6}$$

where ε_0 (= 8.854×10^{-12} F/m) is the permittivity of vacuum, ε_r is the dielectric constant of PEO coatings, d is the thickness of PEO coatings, and S is the testing area. Thus, the dielectric constants (ε_r) of different PEO coatings could be calculated in accordance with formulas (5) and (6).
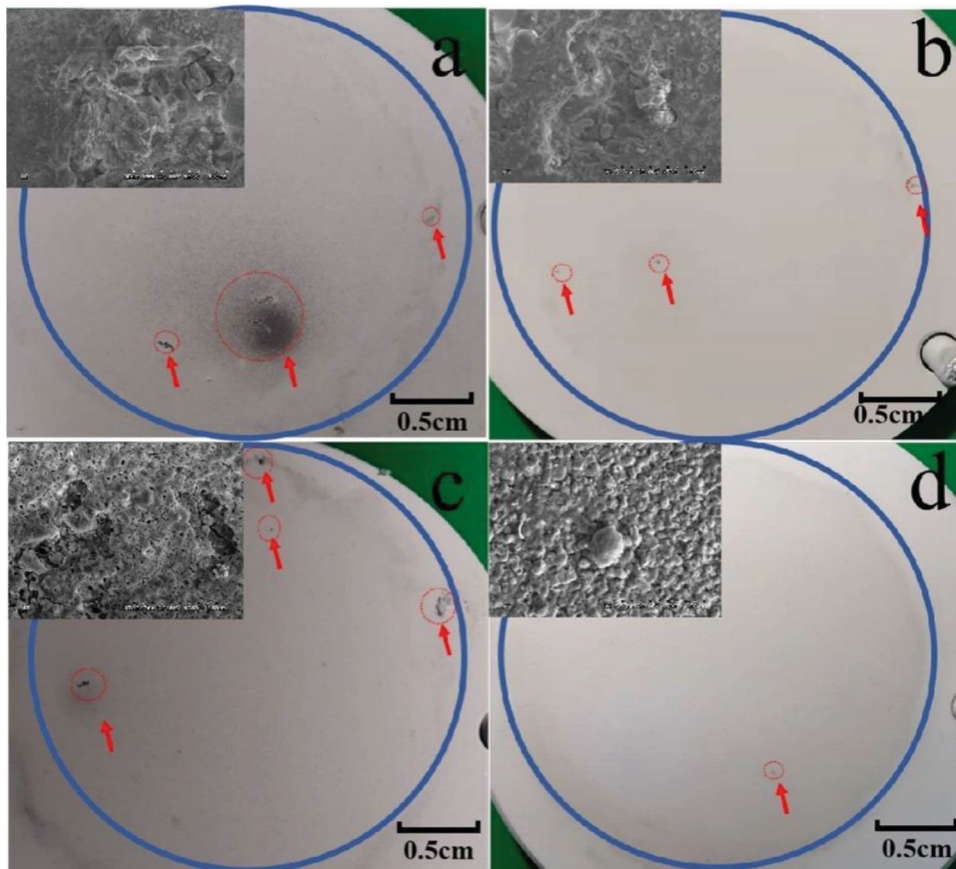
Fig. 11. Morphologies of PEO specimens after immersed in a 3.5% NaCl solution for 50 h (a) coating A; (b) coating B; (c) coating C; (d) coating D

After PEO specimens were immersed in a 3.5 wt.% NaCl solution for 1 h, the ε_r value of PEO coating B, C, D decreased with the oxidation time (Fig. 12). The ε_r values were higher than the dielectric constants of MgO (the ε_r value of MgO was about 10) (Ref 52) because the corrosive media permeated into PEO coatings. It was indicated that the volumes of corrosive media, which penetrated into PEO coatings, were different. Comparatively, the volume of corrosive media in coating D was the lowest, further showing that the porosity of coating D was the smallest. Therefore, the barrier property of PEO coatings depended on the porosity of PEO coatings. In other words, the corrosion resistance of PEO coatings was very associated with their microstructures induced by the distribution of micro-defects in PEO coatings.

In summary, the micro-defects distributed in PEO coatings would provide a transportation path for corrosive media during corrosion. At the initial immersion stage, the through-pores that existed in coating A would provide pathways for corrosive media to reach the coating/substrate interface directly, resulting in the localized corrosion of PEO Mg alloys. Therefore, the increment of the thicknesses of PEO coatings (coating B, C, and D) would be beneficial to improve their effective barrier properties.

During corrosion media transported to the coating/substrate interface through the micro-defects in PEO coatings, corrosive media corroded the internal surface of micro-defects; corrosion products ($Mg(OH)_2$) formed in these micro-defects would
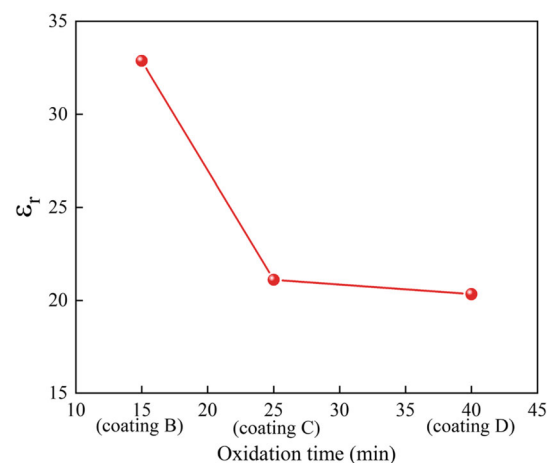
Fig. 12. ε_r values of PEO coatings after immersed for 1 h

generate the internal stress in PEO coatings because of volume expansion (Ref 53, 54). Finally, some through-paths for the transportation of corrosive media in PEO coatings were generated (Ref 28). Thus, localized corrosion occurred to PEO Mg alloys once corrosion media reached the coating/substrate interface. Therefore, there were obvious effects of the microstructures of PEO coatings on the corrosion resistance of PEO Mg alloys.

4. Conclusions

The microstructures in the thickening of PEO coatings were studied using SEM, CLSM in conjunction with XRT. The effects of the microstructures of PEO coatings on the corrosion resistance of PEO Mg alloys were investigated using EIS. The following results were concluded.

(1) The micropores and micro-cracks with different sizes and shapes were distributed stochastically in PEO coatings. During the thickening of PEO coatings, the micropores would develop and connect with each other simultaneously, resulting in the increment of the average diameters of the micropores in PEO coatings. The thickness of PEO coatings gradually increased with oxidation time and the through-pore in PEO coatings would be diminished. The local porosity in PEO coatings increased along the thickness direction of PEO coatings from the coating/substrate interface to the coating surface. But the local porosity of the surface layer of PEO coatings decreased a little due to the surface shrinkage.

(2) There were obvious effects of the microstructures on the corrosion resistance of PEO coatings. The PEO Mg alloy specimens prepared by controlling 40 min of oxidation time exhibited a better corrosion resistance because of their larger thicknesses, denser structure, and higher content of the Mg_2SiO_4 phase.

(3) When PEO Mg alloy specimens were immersed in a 3.5% NaCl solution, the features of their EIS spectra changed with immersion time, showing different corrosion processes occurred to the PEO Mg alloy. The limit value of the low-frequency impedance (R_l) was used to evaluate the corrosion resistance of the PEO Mg alloy in a 3.5% NaCl solution. The evaluation results were verified by corrosion morphologies of the PEO Mg alloy specimens after these specimens were immersed in a 3.5% NaCl solution for 50 h.

References

1. N. Eslamzadeh, R. Ebrahimi-Kahrizsangi, S. Karbasi, A. Zarebidaki and F. Gharavi, An Investigation into the Corrosion Behavior of MgO/ZrO₂ Nanocomposite Coatings Prepared by Plasma Electrolytic Oxidation on the AZ91 Magnesium Alloy, *J. Mater. Eng. Perform.*, 2017, **26**(9), p 4255–4264

2. G. Duan, L. Yang, S. Liao, C. Zhang, X. Lu, Y. Yang, B. Zhang, Y. Wei, T. Zhang and B. Yu, Designing for the Chemical Conversion Coating with High Corrosion Resistance and Low Electrical Contact Resistance on AZ91D Magnesium Alloy, *Corros. Sci.*, 2018, **135**, p 197–206

3. T. Zheng, Y. Hu, F. Pan, Y. Zhang and A. Tang, Fabrication of Corrosion-Resistant Superhydrophobic Coating on Magnesium Alloy by One-Step Electrodeposition Method, *J. Magnes. Alloys*, 2019, **7**(2), p 193–202

4. H. Pokhmurska, B. Wielage, T. Lampke, T. Grund, M. Student and N. Chervinska, Post-treatment of Thermal Spray Coatings on Magnesium, *Surf. Coat. Technol.*, 2008, **202**(18), p 4515–4524

5. C. Blawert, W. Dietzel, E. Ghali and G. Song, Anodizing Treatments for Magnesium Alloys and Their Effect on Corrosion Resistance in Various Environments, *Adv. Eng. Mater.*, 2006, **8**(6), p 511–533

6. G.B. Darband, M. Aliofkhazraei, P. Hamghalam and N. Valizade, Plasma Electrolytic Oxidation of Magnesium and Its Alloys: Mechanism, Properties and Applications, *J. Magnes. Alloys*, 2017, **5**(1), p 74–132

7. Z. Qiu, R. Wang, Y. Zhang, Y. Qu and X. Wu, Study of Coating Growth Behavior during the Plasma Electrolytic Oxidation of Magnesium Alloy ZK60, *J. Mater. Eng. Perform.*, 2015, **24**(4), p 1483–1491

8. M. Mohedano, C. Blawert and M. Zheludkevich, Cerium-Based Sealing of PEO Coated AM50 Magnesium Alloy, *Surf. Coat. Technol.*, 2015, **269**, p 145–154

9. L. Chin, C. Chao and D. Macdonald, A Point Defect Model for Anodic Passive Films, *J. Electrochem. Soc.*, 1981, **128**, p 1187–1194

10. D.D. Macdonald and A. Sun, An Electrochemical Impedance Spectroscopic Study of the Passive State on Alloy-22, *Electrochim. Acta*, 2006, **51**(8–9), p 1767–1779

11. Y. Cai, X. Quan, G. Li and N. Gao, Anticorrosion and Scale Behaviors of Nanostructured ZrO₂–TiO₂ Coatings in Simulated Geothermal Water, *Ind. Eng. Chem. Res.*, 2016, **55**(44), p 11480–11494

12. D. Yu, J. Wang, J. Tian, X. Xu, J. Dai and X. Wang, Preparation and Characterization of TiO₂/ZnO Composite Coating on Carbon Steel Surface and Its Anticorrosive Behavior in Seawater, *Compos. B Eng.*, 2013, **46**, p 135–144

13. W. Li, W. Xing and N. Xu, Modeling of Relationship Between Water Permeability and Microstructure Parameters of Ceramic Membranes, *Desalination*, 2006, **192**(1–3), p 340–345

14. I. Dehri and M. Erbil, The Effect of Relative Humidity on the Atmospheric Corrosion of Defective Organic Coating Materials: An EIS Study with a New Approach, *Corros. Sci.*, 2000, **42**(6), p 969–978

15. J. Parks and H. Leidheiser Jr., Ionic Migration through Organic Coatings and Its Consequences to Corrosion, *Ind. Eng. Chem. Prod. Res. Dev.*, 1986, **25**(1), p 1–6

16. J. Gao, R. Wang, Z. Zhang, D. Song and X. Li, Effect of Membrane Structure of Waterborne Coatings on the Transport Process of Corrosive Medium, *Prog. Org. Coat.*, 2018, **124**, p 8–15

17. P. Xu, C. Zhang, W. Wang and L. Liu, Pitting Mechanism in a Stainless Steel-Reinforced Fe-Based Amorphous Coating, *Electrochim. Acta*, 2016, **206**, p 61–69

18. L.-J. Bai, G. Kou, K. Zhao, G.-T. Chen and F.-X. Yan, Effect of In-Situ Micro-arc Oxidation Coating on the Galvanic Corrosion of AZ31Mg Coupled to Aluminum Alloys, *J. Alloys Compd.*, 2019, **775**, p 1077–1085

19. U. Zerbst, M. Madia, C. Klinger, D. Bettge and Y. Murakami, Defects as a Root Cause of Fatigue Failure of Metallic Components. I: Basic Aspects, *Eng. Fail. Anal.*, 2019, **97**, p 777–792

20. U. Zerbst, M. Madia, C. Klinger, D. Bettge and Y. Murakami, Defects as a Root Cause of Fatigue Failure of Metallic Components. II: Nonmetallic Inclusions, *Eng. Fail. Anal.*, 2019, **98**, p 228–239

21. D.-E. Jiang, B.G. Sumpter and S. Dai, Unique Chemical Reactivity of a Graphene Nanoribbon's Zigzag Edge, *J. Chem. Phys.*, 2007, **126**(13), p 134701

22. S. Deng and V. Berry, Wrinkled, Rippled and Crumpled Graphene: An Overview of Formation Mechanism, Electronic Properties, and Applications, *Mater. Today*, 2016, **19**(4), p 197–212

23. M. Schriver, W. Regan, W.J. Gannett, A.M. Zaniewski, M.F. Crommie and A. Zettl, Graphene as a Long-Term Metal Oxidation Barrier: Worse than Nothing, *ACS Nano*, 2013, **7**(7), p 5763–5768

24. Y. Wu, X. Zhu, W. Zhao, Y. Wang, C. Wang and Q. Xue, Corrosion Mechanism of Graphene Coating with Different Defect Levels, *J. Alloys Compd.*, 2019, **777**, p 135–144

25. V. Sobolev and J. Guilemany, Investigation of Coating Porosity Formation during High Velocity Oxy-Fuel (HVOF) Spraying, *Mater. Lett.*, 1994, **18**(5–6), p 304–308

26. S. Zhang, J. Wu, W. Qi and J. Wang, Effect of Porosity Defects on the Long-Term Corrosion Behaviour of Fe-Based Amorphous Alloy Coated Mild Steel, *Corros. Sci.*, 2016, **110**, p 57–70

27. N. Xiang, R. Song, H. Li, C. Wang, Q. Mao and Y. Xiong, Study on Microstructure and Electrochemical Corrosion Behavior of PEO Coatings Formed on Aluminum Alloy, *J. Mater. Eng. Perform.*, 2015, **24**(12), p 5022–5031

28. Z. Chen, H. Ji, X. Geng, X. Chen, X. Yong and S. Zhang, 3-D Distribution Characteristics of the Micro-defects in the PEO Coating on ZM6 mg-Alloy during Corrosion, *Corros. Sci.*, 2020, **174**, 108821

29. L. Pezzato, L.B. Coelho, R. Bertolini, A.G. Settimi, K. Brunelli, M. Olivier and M. Dabalà, Corrosion and Mechanical Properties of Plasma Electrolytic Oxidation-Coated AZ80 Magnesium Alloy, *Mater. Corros.*, 2019, **70**(11), p 2103–2112

30. L. Pezzato, L. Lorenzetti, L. Tonelli, G. Bragaggia, M. Dabalà, C. Martini and K. Brunelli, Effect of SiC and Borosilicate Glass Particles on the Corrosion and Tribological Behavior of AZ91D Magnesium Alloy After PEO Process, *Surf. Coat. Technol.*, 2021, **428**, 127901

31. M.B. Kannan, P. Lenin, H. Khakbaz and R.-C. Zeng, *Recent Approaches for Enhancing Corrosion Resistance of PEO/MAO-Coated Mg and Its Alloys, Conversion Coatings for Magnesium and Its Alloysed*, Springer, 2022, p 465–488

32. Y. Gu, S. Bandopadhyay, C.-F. Chen, Y. Guo and C. Ning, Effect of Oxidation Time on the Corrosion Behavior of Micro-arc Oxidation Produced AZ31 Magnesium Alloys in Simulated Body Fluid, *J. Alloys Compd.*, 2012, **543**, p 109–117

33. R. Hussein, X. Nie and D. Northwood, An Investigation of Ceramic Coating Growth Mechanisms in Plasma Electrolytic Oxidation (PEO) Processing, *Electrochim. Acta*, 2013, **112**, p 111–119

34. H. Wang, Z. Chen and L. Li, Corrosion Resistance and Microstructure Characteristics of Plasma Electrolytic Oxidation Coatings Formed on AZ31 Magnesium Alloy, *Surf. Eng.*, 2010, **26**(5), p 385–391

35. C. Blawert, V. Heitmann, W. Dietzel, H. Nykyforchyn and M. Klapkiv, Influence of Process Parameters on the Corrosion Properties of Electrolytic Conversion Plasma Coated Magnesium Alloys, *Surf. Coat. Technol.*, 2005, **200**(1–4), p 68–72

36. H.S. Ryu, S.-J. Mun, T.S. Lim, H.-C. Kim, K.-S. Shin and S.-H. Hong, Microstructure Evolution during Plasma Electrolytic Oxidation and Its Effects on the Electrochemical Properties of AZ91D Mg Alloy, *J. Electrochem. Soc.*, 2011, **158**(9), p C266

37. A. Madhan Kumar, S. Hwan Kwon, H. Chul Jung, Y.H. Park, H.J. Kim and K.S. Shin, Fabrication and Electrochemical Corrosion Behavior of PEO Coatings on Strip-Cast AZ31Mg Alloy in 3.5% NaCl Solution, *Ind. Eng. Chem. Res.*, 2014, **53**(23), p 9703–9713

38. L. Zhang and S. Wang, Correlation of Materials Property and Performance with Internal Structures Evolvement Revealed by Laboratory X-Ray Tomography, *Materials*, 2018, **11**(10), p 1795

39. X. Zhang, S. Aliasghari, A. Nemcova, T.L. Burnett, I. Kubena, M. Smid, G.E. Thompson, P. Skeldon and P.J. Withers, X-Ray Computed Tomographic Investigation of the Porosity and Morphology of Plasma Electrolytic Oxidation Coatings, *ACS Appl. Mater. Interfaces*, 2016, **8**(13), p 8801–8810

40. X. Lu, C. Blawert, D. Tolnai, T. Subroto, K.U. Kainer, T. Zhang, F. Wang and M.L. Zheludkevich, 3D Reconstruction of Plasma Electrolytic Oxidation Coatings on Mg Alloy via Synchrotron Radiation Tomography, *Corros. Sci.*, 2018, **139**, p 395–402

41. M. Kaseem, S. Fatimah, N. Nashrah and Y.G. Ko, Recent Progress in Surface Modification of Metals Coated by Plasma Electrolytic Oxidation: Principle, Structure, and Performance, *Prog. Mater. Sci.*, 2020, **117**, p 100735

42. E. Cakmak, K.C. Tekin, U. Malayoglu and S. Shrestha, The Effect of Substrate Composition on the Electrochemical and Mechanical Properties of PEO Coatings on Mg Alloys, *Surf. Coat. Technol.*, 2010, **204**(8), p 1305–1313

43. S. Gnedenkov, O. Khrisanfova, A. Zavidnaya, S. Sinebryukhov, V. Egorkin, M. Nistratova, A. Yerokhin and A. Matthews, PEO Coatings Obtained on an Mg-Mn Type Alloy under Unipolar and Bipolar Modes in Silicate-Containing Electrolytes, *Surf. Coat. Technol.*, 2010, **204**(14), p 2316–2322

44. H. Guo, M. An, H. Huo, S. Xu and L. Wu, Microstructure Characteristic of Ceramic Coatings Fabricated on Magnesium alloys by Micro-arc Oxidation in Alkaline Silicate Solutions, *Appl. Surf. Sci.*, 2006, **252**(22), p 7911–7916

45. B. Hinderliter, S. Croll, D. Tallman, Q. Su and G. Bierwagen, Interpretation of EIS Data from Accelerated Exposure of Coated Metals Based on Modeling of Coating Physical Properties, *Electrochim. Acta*, 2006, **51**(21), p 4505–4515

46. M.T. Tran, B. Tribollet, V. Vivier and M.E. Orazem, On the Impedance Response of Reactions Influenced by Mass Transfer, *Russ. J. Electrochem.*, 2017, **53**(9), p 932–940

47. Z. Li, L. Zhang, I. Udoh, A. Ma and Y. Zheng, Deformation-Induced Martensite in 304 Stainless Steel During Cavitation Erosion: Effect on Passive Film Stability and the Interaction Between Cavitation Erosion and Corrosion, *Tribol. Int.*, 2022, **167**, p 107422

48. C. Yu, L.-Y. Cui, Y.-F. Zhou, Z.-Z. Han, X.-B. Chen, R.-C. Zeng, Y.-H. Zou, S.-Q. Li, F. Zhang and E.-H. Han, Self-Degradation of Micro-arc Oxidation/Chitosan Composite Coating on Mg-4Li-1Ca Alloy, *Surf. Coat. Technol.*, 2018, **344**, p 1–11

49. Y. Xia, B. Zhang, C. Lu and L. Geng, Improving the Corrosion Resistance of Mg-4.0Zn-0.2Ca Alloy by Micro-arc Oxidation, *Mater. Sci. Eng. C*, 2013, **33**(8), p 5044–5050

50. Z. Lin, Y. Zhao, P.K. Chu, L. Wang, H. Pan, Y. Zheng, S. Wu, X. Liu, K.M. Cheung and T. Wong, A Functionalized TiO_2/Mg_2TiO_4 Nano-layer on Biodegradable Magnesium Implant Enables Superior Bone-Implant Integration and Bacterial Disinfection, *Biomaterials*, 2019, **219**, 119372

51. C. Hsu and F. Mansfeld, Technical Note: Concerning the Conversion of the Constant Phase Element Parameter Y0 into a Capacitance, *Corrosion*, 2001, **57**, p 747–748

52. G. Baril, G. Galicia, C. Deslouis, N. Pébère, B. Tribollet and V. Vivier, An Impedance Investigation of the Mechanism of Pure Magnesium Corrosion in Sodium Sulfate Solutions, *J. Electrochem. Soc.*, 2006, **154**(2), p C108

53. S. Xia, R. Yue, R. Rateick Jr. and V. Birss, Electrochemical Studies of AC/DC Anodized Mg Alloy in NaCl Solution, *J. Electrochem. Soc.*, 2004, **151**(3), p B179

54. H. Duan, K. Du, C. Yan and F. Wang, Electrochemical Corrosion Behavior of Composite Coatings of Sealed MAO Film on Magnesium Alloy AZ91D, *Electrochim. Acta*, 2006, **51**(14), p 2898–2908